Tutorial 16:

Thermal imaging in semi-transparent media

S. Chevalier[1,2], **C. Bourgès**[1,2], **J. Maire**[1,2], **A. Sommier**[1,2], **C. Pradère**[3], **S. Dilhaire**[4]

1. ENSAM, CNRS, Bordeaux INP, I2M, UMR 5295, F-33400 Talence, France
2. Univ. Bordeaux, CNRS, Bordeaux INP, I2M, UMR 5295, F-33400, Talence, France
3. EPSILON-ALCEN, F-33400 Talence, France
4. Univ. Bordeaux, CNRS, LOMA, UMR 5798, F-33400 Talence, France

E-mail: stephane.chevalier@u-bordeaux.fr
coline.bourges@u-bordeaux.fr
jeremie.maire@u-bordeaux.fr

Abstract. Modulated thermotransmittance infrared imaging is a non-destructive method for measuring thermal properties and temperature fields in semi-transparent media. It differs from IR thermography as it does not require knowledge of the material's emissivity and can achieve spatial resolutions down to 10 µm/px. Through this experimental tutorial, we propose to measure the heat diffusivity and the thermal field in a glass wafer. After a brief description of the setup and the demodulation technique, the analytical model of the temperature will be derived and used in an inverse method to measure the borofloat thermal diffusivity.

Scope

1 Introduction

In this tutorial work, the semitransparent materials under study are non-scattering at their surface as their roughness is much lower than the illumination wavelength $\lambda \in [2-6]$ µm, and the reflectance at their surface is considered specular. All our samples are double-side polished to remain in this working hypothesis. In addition, we use homogeneous materials, whose scattering in the volume is negligible compared to the absorbance. We develop the experiment mainly using a double-side polished glass wafer. In addition, these materials can reflect or absorb a part of the incident light, as shown in Figure 1.

We present some contactless methods to measure temperature of semitransparent materials, without coating them. First, we introduce the IRT applied to semitransparent media and the associated issue to measure the temperature field. Second, we detail the principle of thermo-transmittance.

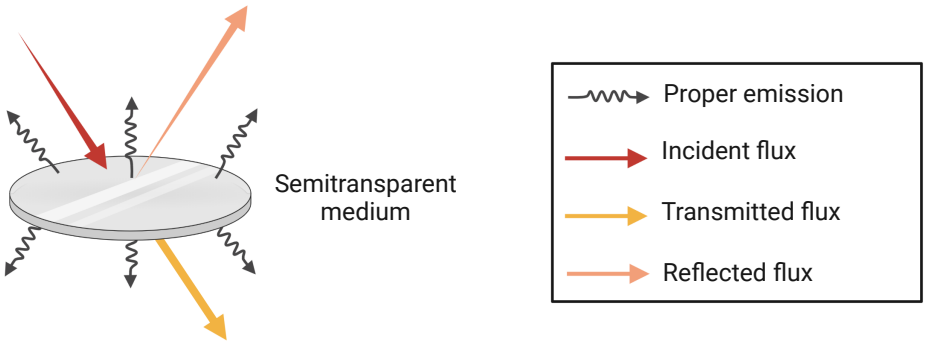

Figure 1: IR radiations interactions with a semitransparent medium.

IRT applied to semitransparent materials

Measuring temperature in semitransparent media using IRT is much more challenging than in opaque ones. The proper emission comes from the two material surfaces, but also from its volume. The emissivity is no longer defined for these materials: one uses the apparent emissivity [1] or emittance [2]. In addition, it is essential to consider the radiations from the environment, which are reflected, absorbed, and transmitted through the material [3].

Because of these challenges, IRT in semitransparent media is not yet widely used, although several groups are interested in it and develop specific calibration processes. For instance, some works measured the emittance, such as [3, 4, 5, 6], but the definition may vary from one study to another, and not always take into account the direction of radiations. Other works focused on thermal properties measurements of these materials, such as the thermal diffusivity [7]. In this thesis work, we propose an alternative method that does not require the knowledge of the emittance of the medium and allows to discriminate the signal of interest from the radiation coming from the environment.

Thermotransmittance

We introduce the thermotransmittance phenomenon, by establishing the link between temperature dependence of the transmitted light in non-opaque materials [8]. As a consequence, to measure temperature using thermotransmittance, we need the proportionality factor: the

thermotransmittance coefficient κ (K^{-1}). Unfortunately, there is no database on the coefficient κ. This property is often measured but mostly in the visible or NIR range [9].

Preliminary studies reported promising results in calibrating the thermotransmittance coefficient for various materials across different spectral ranges, including mid-infrared [10] and terahertz [11]. Additionally, works demonstrated the temperature dependency of absorbance in water-ethanol mixtures within the near-infrared spectrum [12]. As the thermotransmittance signal is affected by both absorbance and reflectance variations (see section 2), it has potential applications for diverse semitransparent media, providing either a measurement of thermoreflectance, thermo-absorbance, or a combination of both. Finally, these studies showed that the thermal dependency of absorbance/transmittance varies with the illumination wavelength. As a result, it should be possible to differentiate several components of a semitransparent media depending on their thermotransmittance coefficient behavior as a function of the wavelength, provided the initial spectrum of each component is known.

However, the thermotransmittance coefficient in the mid-IR is usually weak, about 10^{-4} K^{-1}. Therefore, it is essential to heat the sample sufficiently and use sensitive detectors (in the work [10] $\Delta T = 120$ K and detector with a dynamic range of 2^{16}).

The objectives of this tutorial are as follows:

1. to measure the thermotransmittance in a semi-transparent media from an IR beam;
2. to estimate the heat diffusivity in the bulk of the semi-transparent media.

2 Thermotransmittance working principle and modeling

This section describes the working principle of thermotransmittance. First, the transmitted signal through a non-scattering media is detailed. Second, we introduce the thermal dependence of this signal and present the working hypotheses.

Transmittance of a semitransparent material

When a monochromatic incident flux Φ_0 illuminates a semitransparent material, a part of the flux is reflected at the material surface, and a part is transmitted through the sample [13] depending on the reflectance coefficient R_0, as illustrated in Figure 2. As it passes through the medium, the flux is attenuated by the attenuation coefficient α_0 (m^{-1}) within the thickness L_z (m) of the material. At ambient temperature, the transmitted flux is written $\Phi_\Gamma = \Phi_0 \Gamma_0$, with Γ_0 the transmittance of the material which is expressed in the following equation.

$$\Gamma_0 = [1 - R_0]^2 e^{-\int_0^{L_z} \alpha_0(z) dz} \tag{1}$$

Expression of the thermotransmittance

Since the optical properties of a material vary with temperature, we express the equation 1 as a function of temperature in the general case, where both surfaces of the sample are not necessarily at the same temperature.

$$\Gamma(T) = \underbrace{[1 - R(T_1)]}_{\text{Surface 1}} \underbrace{[1 - R(T_2)]}_{\text{Surface 2}} \underbrace{e^{-\int_0^{L_z} \alpha(z, T_z) dz}}_{\text{Volume}} \tag{2}$$

The thermal dependency of transmittance comes from both the reflectance and the attenuation coefficient. At the first order, their temperature variations are expressed in the equations 3

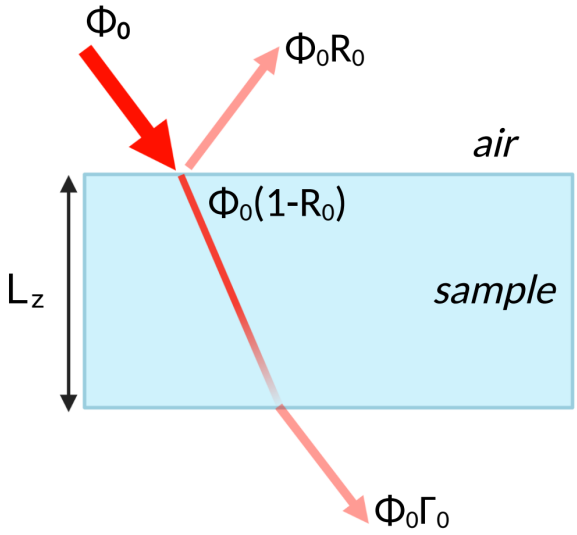

Figure 2: Illustration of a light beam path in a semitransparent medium.

and 4, with $\Delta T = T - T_0$ the temperature variation, κ_R the thermoreflectance coefficient (K^{-1}), and κ_α the thermo-absorbance coefficient (K^{-1}).

$$R(T) = R_0[1 + \kappa_R \Delta T] \tag{3}$$
$$\alpha(T) = \alpha_0[1 + \kappa_\alpha \Delta T] \tag{4}$$

By injecting 3 and 4 in the expression 2 and linearizing the exponential term, the thermo-transmittance relation at first order is given in the following expression.

$$\frac{\Delta\Gamma(T)}{\Gamma_0} \approx \underbrace{-\frac{R_0\kappa_R}{1-R_0}\left[\Delta T_1 + \Delta T_2\right]}_{\text{reflectance}} \underbrace{-\alpha_0\kappa_\alpha \int_0^{L_z} \Delta T(z)dz}_{\text{absorbance}} \tag{5}$$

As a result, the reflectance part gives information about the temperature variations at the surfaces of the sample, whereas the absorbance provides information on the temperature gradient through the thickness. In this tutorial we limit the study to uniform temperature along the material thickness ($\Delta T_1 = \Delta T_2 = \langle \Delta T \rangle_z = \Delta T$). The thermotransmittance has therefore a simple expression:

$$\frac{\Delta\Gamma(T)}{\Gamma_0} = \kappa \Delta T \tag{6}$$

κ is the thermotransmittance coefficient (K^{-1}) which contains both absorbance and reflectance thermal dependencies.

3 Modulated thermotransmittance imaging experimental setup

Figure 3 illustrates the experimental setup for modulated thermotransmittance imaging. The thermal modulation of the sample has great advantage to increase the signal to noise ratio by filtering the noise from images in order to detect the weak thermotransmittance signal.

In the experimental setup, we use the IR source, the mechanical chopper for modulating the source, the annular Peltier module for heating the sample, and an infrared camera as detector. The double-demodulation is post-processed, and the operations are detailed in section 4.

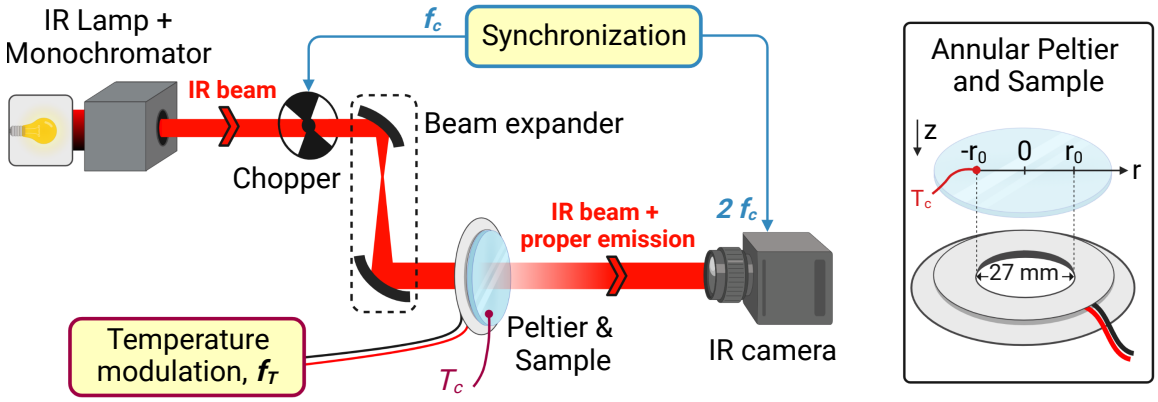

Figure 3: Experimental setup for modulated thermotransmittance imaging measurement. The insert illustrates the Peltier module with its dimensions.

Heating of the sample

The sample is heated using a ring-shaped Peltier module. The temperature at the edges of the wafer is modulated at $T(t) = T_0 + \Delta T \cos(2\pi f_T t)$, with $T_0 \sim 20°C$, $\Delta T \sim 10°C$. We will choose the modulation frequency f_T in the order of tens mHz for Borofloat wafer.

Infrared camera properties

We use an infrared camera as detector (FLIR SC7000). The camera has an Indium-antimonide sensor composed of 256 x 320 pixels with a pitch of 30 μm. The focal length of the objective is 50 mm, and the spatial resolution of the images recorded by the camera around 200 μm/pixel. In addition, the camera spectral sensitivity range is $\lambda \in [2.5 - 5.5]\ \mu m$. Figure 4 plots the normalized spectral sensitivity of the acquisition system, which includes the spectral responses of the camera, the lens objective, the air absorption, and the IR lamp emission. We are not able to differentiate the different contributions with the available equipment. However, the absorption peak at $\lambda = 4300$ nm is the signature of the CO_2 in the air [14]. In this tutorial, polychromatic light integrated over the spectral range of the camera is used to increase the SNR.

The signal measured by each pixel, $U_{\text{pix}}(t)$, is directly proportional to the total flux $\Phi_{\text{tot}}(t)$ it receives. Depending on the received flux, each pixel generates an electrical signal: $U_{\text{pix}} = \rho_{\text{pix}}\Phi_{\text{tot}}$, with ρ_{pix} a proportionality factor specific to each pixel since they are all slightly different (size, noise, offset, ...). To compensate for these differences, we perform a non-uniformity correction (NUC) before starting the measurements [15]. The method consists in taking several images of a black body covering the entire field of view of the camera. After calculating the temporal and spatial average of the signal, a correction coefficient is applied to each pixel. This operation is performed by the software of the camera (Altair).

In addition, the IR camera converts the voltage signal of each pixel in digital levels (DL). Since the camera has a dynamic range of 14 bits, the pixel value is in the range [0 ; 2^{14}-1] DL. If the incident flux is too intense, the pixel is saturated, and its value is theoretically 16 383

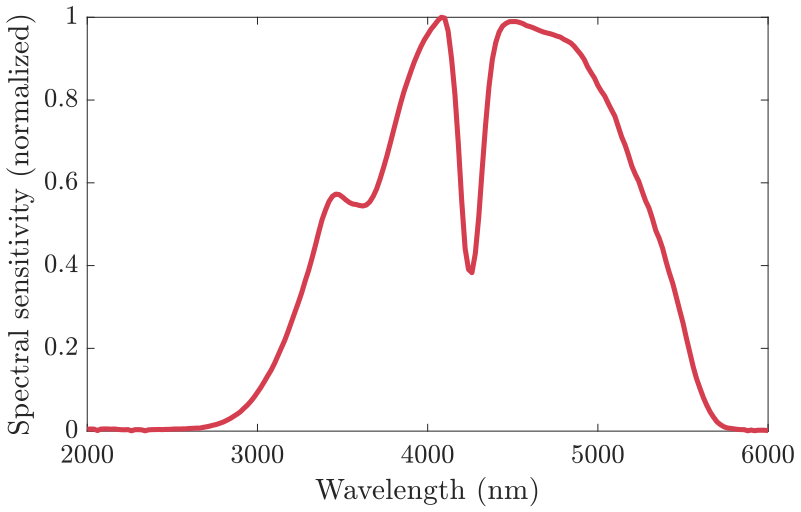

Figure 4: Spectral sensitivity of the acquisition chain, measured by scanning the wavelength with the monochromator. The peak around $\lambda = 4300$ nm corresponds to the CO_2 absorption.

DL. However, the upper limit of the camera operating range is 14 000 DL. Beyond that, the incident flux and pixel value are no longer proportional, and the signal should be saturated. In addition, below 2 000 DL, the camera does not operate optimally either. Therefore, always be sure to work in the [2 000 - 14 000] DL range.

Finally, a Stirling cools the camera to a temperature of $T_{\mathrm{CAM}} \approx 79$ K. As long as the camera is not properly cooled, the recorded signal is not stable enough. Figure 5 shows the drift of the measured signal over time. We propose to determine this drift by placing an ambient black body at 30 cm in front of the camera and regularly recording the measured signal. The sensor is only stable after two hours of operation: the measured signal at $t = 200$ min varies by more than 5% compared to the beginning of the measurement. That shows the importance of letting the camera cool down for at least two hours before making the measurements. Working with modulated signals reduces the impact of the camera drift on the results.

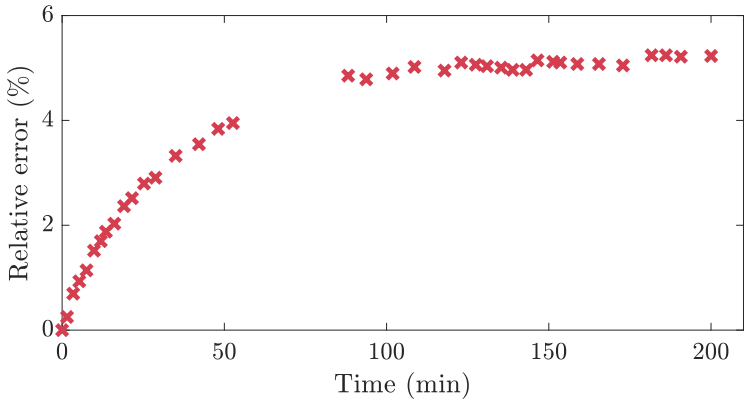

Figure 5: Drift of the signal recorded by the camera over time, measured on a ROI of 50x50 pixels.

Mechanical chopper settings

In this setup, the camera is synchronized with the mechanical chopper to record one frame when the chopper cuts the IR beam, and another when the light passes through the sample [16]. The only requirement for the chopper frequency f_c is $f_c \gg f_T$ to properly remove the proper emission of the sample. We choose $f_c = 11$ Hz, and the camera acquisition frame rate is $f_{\text{cam}} = 22$ Hz. The output signal of each pixel of the camera is given in the equation 7: the IR transmitted signal is only measured every other frame, at the frequency f_c. $\mathcal{C}(t)$ is the chopper rectangular wave function equals to 1 when the IR beam passes through the sample, and 0 when it is cut. The next section presents the double-demodulation method, applied on the images recorded by the camera.

$$U_{\text{pix}}(t) = \rho_{\text{pix}} \left[\Phi_0 \Gamma_0 (1 + \kappa \Delta T \cos(2\pi f_T t)) \mathcal{C}(t) + E(T,t)\right] \tag{7}$$

$$\begin{cases} \mathcal{C}(t) = 0, \text{ when the chopper cuts the IR beam} & (8) \\ \mathcal{C}(t) = 1, \text{ when the IR beam passes through the sample} & (9) \end{cases}$$

4 Double-demodulation method applied on images

As mentioned in the introduction, we use the two-image method, subtracting the proper emission thanks to the synchronization of the camera with the chopper.
The presented methods allow us to demodulate simultaneously the signal recorded by all the pixels of the camera. We do not work in real time but post process the films recorded during the experiment.

4.1 Proper emission subtraction: the two-image method

As mentioned, the camera is synchronized with the mechanical chopper to discriminate the transmitted flux $\Phi_0\Gamma(t)$ from the parasitic signal $E(t)$. The camera successively records one frame when the chopper lets the light passing through the sample (U_{on}) and another when it cuts the light beam (U_{off}). The frequency of the camera is $f_{\text{cam}} = 2f_c$ with f_c the chopper frequency, we define $\tau_c = 1/f_c$. The difference between two consecutive frames results in equation 10.

$$U_{\text{on}}(t) - U_{\text{off}}(t + \frac{\tau_c}{2}) = \rho_{\text{pix}} \Phi_0 \Gamma_0 [1 + \kappa \Delta T \cos(2\pi f_T t)] + \Delta_{\text{res}} \tag{10}$$

The term Δ_{res} is the residuals of the parasitic radiations and noise measurement after the subtraction: $\Delta_{\text{res}} = E(t) - E(t + \frac{\tau_c}{2})$. These residuals are negligible compared to the thermotransmittance signal, providing some conditions: the proper emission must be constant between two consecutive frames, otherwise the residual Δ_{res} depends on the temperature, and the source demodulation is not correctly performed. This is why the chopper frequency, f_c, is set much higher than the thermal frequency, f_T. The first experimental measurement is to check if the proper emission is correctly removed with the chosen frequencies (f_T, f_c).
Figure 6 shows the two-image method on two consecutive images recorded by the IR camera, when the IR flux passes through the sample (a) and when it is cut by the chopper (b). The subtraction of the two images results in frame (c). As mentioned in section 3, the camera has a limited dynamic range of 14 bits. Since all the parasitic radiations are added to the useful IR transmitted flux, the remaining signal after two-image subtraction may be weak. So, we understand the interest of maximizing the IR flux compared to the unwanted radiations. Several strategies are possible:

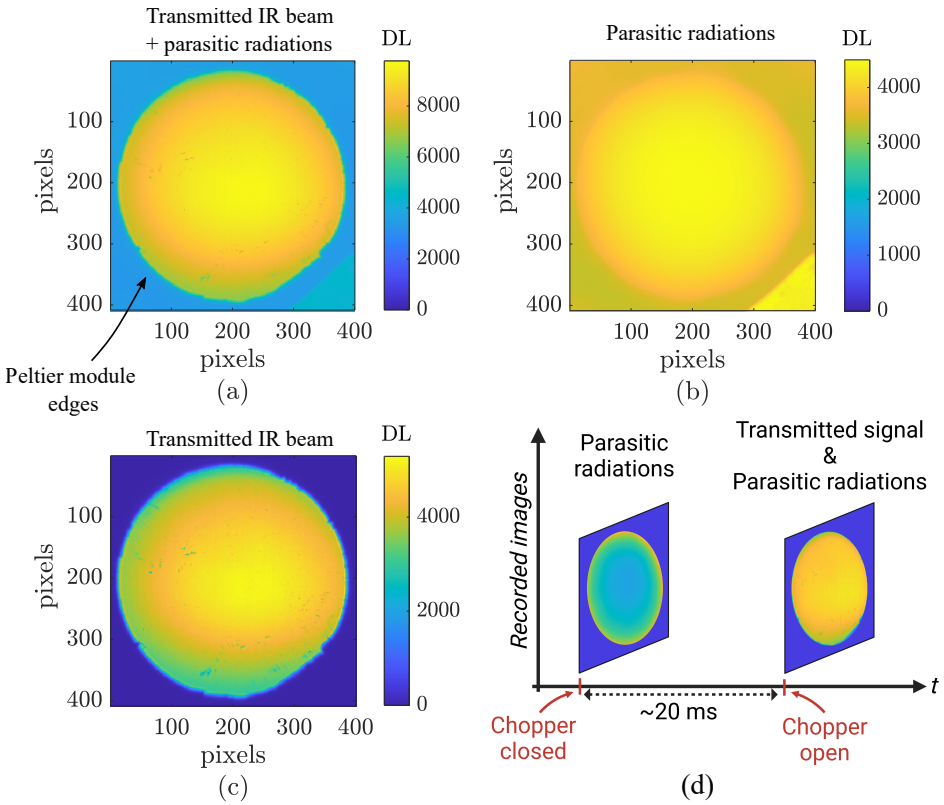

Figure 6: Images of (a) IR transmitted beam with proper emission, $U_{\text{on}}(t)$, (b) proper emission and parasitic radiations, $U_{\text{off}}(t + \frac{\tau_c}{2})$, and (c) IR beam after proper emission subtraction, $U_{\text{on}}(t) - U_{\text{off}}(t + \frac{\tau_c}{2})$. (d) Illustration of the two-image process.

- As we cannot influence the proper emission of the sample, we must operate on the IR incident beam. One possibility is to concentrate its power. The higher the intensity of the transmitted beam, the more we can decrease the integration time of the camera and, thus, the component of the proper emission.
- The wavelength of the IR beam is chosen where the measured IR transmitted beam is maximal. This wavelength depends on the camera sensitivity and the transmittance of the sample.
- We can use an IR bandpass filter between the sample and the camera. That eliminates the components of the proper emission outside the filter. The filter must be adapted to the wavelength of the IR beam.

Using a filter generates parasitic reflections, attenuates the transmitted IR beam, and must be changed according to the wavelength. As a consequence, we will focus on the first two points for the following. Finally, after the two-image subtraction, we get the signal $U_{\text{pix,IR}}(t)$ at the chopper frequency f_c.

$$U_{\text{pix,IR}}(t) = \rho_{\text{pix}} \Phi_0 \Gamma_0 [1 + \kappa \Delta T \cos(2\pi f_T t)] + \Delta_{\text{res}} \tag{11}$$

4.2 Demodulation of the transmitted signal

A numerical demodulation is used to obtain the module and phase from the thermotransmittance. A Fast Fourier Transform (FFT) algorithm in Matlab is employed to process the

image. These, in each pixel of the image we obtain the module:

$$\|\Delta U_{\text{pix,IR}}(\omega = 2\pi f_T)\| = \rho_{\text{pix}} \Phi_0 \Gamma_0 \kappa \Delta T, \tag{12}$$

and the thermotransmittance phase

$$\arg(\Delta U_{\text{pix,IR}}(\omega = 2\pi f_T)) = \hat{\phi} \tag{13}$$

These two quantities can be used to estimate the heat diffusivity, convective coefficient, or to calibrate the thermotransmittance coefficient κ over the spectral range of the camera. The demodulation based on FFT requires to record at least 10 periods to ensure a sufficient spectral resolution in the process data. The longer the experiments lasts, the better the precision of the algorithm is.

5 Heat transfer modeling of a thin wafer in cylindrical coordinates

This section studies the heat transfer in a thin silicon wafer heated at its edges by a ring-shaped Peltier module. We calculate the temperature variation ΔT in the sample, and determine the operating modulation frequency f_T.

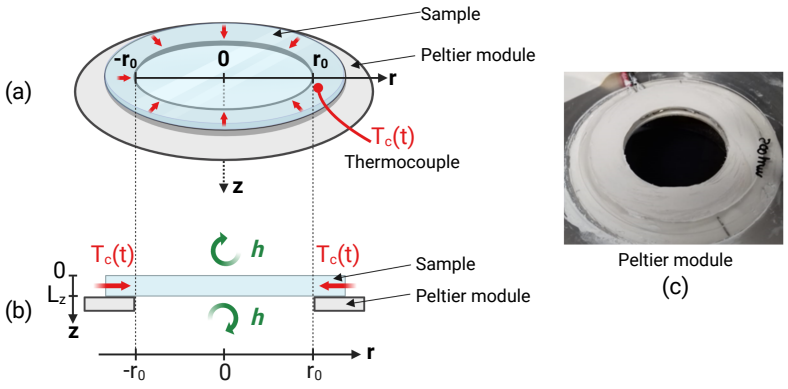

Figure 7: Illustration of the heat transfer problem. (a) 3D view of the Peltier module and the sample heated to a modulated temperature $T_c(t)$. (b) Cross-sectional view with boundary conditions. (c) Image of the Peltier module.

5.1 Solving the heat transfer equation

The shape of the heating system is important to let the incident flux Φ_0 passing through the sample. The sample and the Peltier module are positioned vertically. Figure 7 illustrates the geometry of the problem with the boundary conditions. Let's consider a sample of radius r_0 (m) and thickness L_z (m), of thermal diffusivity a (m^2/s) and thermal conductivity k (W/m/K). Due to the geometry of the wafer and the heating system, we use the cylindrical coordinate system (r, ϑ, z). As the sample is homogeneously heated at its edges, we do not consider the azimuth coordinate ϑ: the temperature does not depend on the angle ϑ. The final coordinate system is (r, z).

Boundary conditions

The temperature is set to the modulated temperature $T(t) = T_0 + \Delta T \cos(\omega_T t)$ at the edges of the sample ($r = r_0$ and $r = -r_0$), with T_0 the ambient temperature and $\omega_T = 2\pi f_T$ the angular frequency (rad/s). For symmetry reasons, at the position $r = 0$, the radial flux is assumed to be equal to zero. We impose convection losses at the surfaces $z = 0$ and $z = L_z$, with h being the convection coefficient (W/m^2/K). The system of equations [14 to 19] expresses the heat transfer problem in cylindrical coordinates with boundary conditions over time t.

$$\begin{cases} \dfrac{\partial^2 T(r,z,t)}{\partial r^2} + \dfrac{1}{r}\dfrac{\partial T(r,z,t)}{\partial r} + \dfrac{\partial^2 T(r,z,t)}{\partial z^2} = \dfrac{1}{a}\dfrac{\partial T(r,z,t)}{\partial t} & (14) \\ -k \left.\dfrac{\partial T(r,z,t)}{\partial z}\right|_{z=0} = -h(T(r,z=0,t) - T_0) & (15) \\ -k \left.\dfrac{\partial T(r,z,t)}{\partial z}\right|_{z=L_z} = h(T(r,z=L_z,t) - T_0) & (16) \\ \left.\dfrac{\partial T(r,z,t)}{\partial r}\right|_{r=0} = 0 & (17) \\ T(r=r_0,z,t) = T(r=-r_0,z,t) = T_0 + \Delta T(r_0)\cos(\omega_T t) & (18) \\ T(r,z,t=0) = T_0 & (19) \end{cases}$$

Linearization of convective losses

The borofloat thermal conductivity is about $k \approx 1$ W/m/K, its thickness is 500 µm and the convection coefficient is approximately $h \approx 15$ W/m^2/K for the vertical configuration used in the experimental setup. This leads to a Biot number $B_i \approx 2.10^{-2} \ll 1$, which means that the temperature is homogeneous in the sample thickness. As a result, the partial derivative with respect to z can be linearized, as expressed in equation 21. We substitute this result in the previous system of equations.

$$\frac{\partial^2 T(r,z,t)}{\partial z^2} \approx \frac{\left.\frac{\partial T(r,z,t)}{\partial z}\right|_{z=L_z} - \left.\frac{\partial T(r,z,t)}{\partial z}\right|_{z=0}}{L_z} \quad (20)$$

$$\approx -\frac{2h}{kL_z}(T(r,z=L_z,t) - T_0) \quad (21)$$

Temperature decomposition as periodic function

To solve the system, the temperature is decomposed into a constant and a term depending on the angular frequency ω_T:

$$\underline{T}(r,t) = T_0 + \Delta\underline{T}(r,\omega_T)e^{i\omega_T t} \quad (22)$$

With $\Delta\underline{T}(r,\omega_T)$ the complex temperature amplitude at the frequency f_T. After substituting the partial derivative with respect to z and the expression of $\underline{T}(r,t)$, the previous system of equations [14 to 19] becomes:

$$\begin{cases} \dfrac{d^2\Delta\underline{T}(r,\omega_T)}{dr^2} + \dfrac{1}{r}\dfrac{d\Delta\underline{T}(r,\omega_T)}{dr} - \dfrac{2h}{kL_z}\Delta\underline{T}(r,\omega_T) = \dfrac{i\omega_T}{a}\Delta\underline{T}(r,\omega_T) & (23) \\ \left.\dfrac{d\Delta\underline{T}(r,\omega_T)}{dr}\right|_{r=0} = 0 & (24) \\ |\Delta\underline{T}(r=r_0,\omega_T)| = |\Delta\underline{T}(r=-r_0,\omega_T)| = \Delta T(r_0) & (25) \end{cases}$$

Solution of the system

The solution of the system is given in equation 26, with $H = 2h/kL_z$ the loss factor (m^{-2}), $\mathcal{I}_0$ and $\mathcal{K}_0$ the modified Bessel functions of first and second kind.

$$\Delta\underline{T}(r,\omega_T) = A\mathcal{I}_0\left(r\sqrt{H + i\frac{\omega_T}{a}}\right) + B\mathcal{K}_0\left(r\sqrt{H + i\frac{\omega_T}{a}}\right) \quad (26)$$

A and B are determined with the boundary conditions:

- At the center of the wafer, an adiabatic condition is assumed. As the function $\mathcal{K}_1(r)$ tends towards ∞ at $r = 0$, B must be equal to zero to satisfy equation 24.
- At the edge $r = r_0$, the boundary condition gives: $A = \Delta T(r_0)/\mathcal{I}_0\left(r_0\sqrt{H + i\frac{\omega_T}{a}}\right)$.

Finally, the complex temperature field as a function of the position r and the frequency f_T is expressed in equation 27.

$$\Delta\underline{T}(r,\omega_T) = \Delta T(r_0)\frac{\mathcal{I}_0\left(r\sqrt{H + i\frac{\omega_T}{a}}\right)}{\mathcal{I}_0\left(r_0\sqrt{H + i\frac{\omega_T}{a}}\right)} \quad (27)$$

Two quantities are then extracted from this model, the phase $\phi = \arg(\Delta\underline{T}(r,\omega_T))$ and the normalized modulus $\|\Delta\underline{T}(r,\omega_T)\|/\|\Delta\underline{T}(R,\omega_T)\|$.

6 Inverse methods

6.1 Minimization and objective function

The inverse method to estimated a is based here on the minimization between the calculated phase from the model and the measured thermotransmittrance phase. The cost function to be minimised takes into account the error bar on the phase measurements, and writes as

$$\mathcal{J}(a) = (\hat{\boldsymbol{\phi}} - \boldsymbol{\phi}(a))^T \boldsymbol{W}(\hat{\boldsymbol{\phi}} - \boldsymbol{\phi}(a)) \quad (28)$$

where $\boldsymbol{W}$ is a diagonal weight matrix containing the standard deviation of the measurements $\hat{\boldsymbol{\phi}}$. Each element of the diagonal of the matrix is computed as $1/\sigma^2_{\hat{\phi}}$.

A simple gradient method can be used to estimate a. Algorithms such as Levenberg-Marquardt are recommended in Matlab. But here we propose to use the Gauss-Newton algorithm such as

$$a^{k+1} = a^k + [(\boldsymbol{S}^k)^T \boldsymbol{W} \boldsymbol{S}^k]^{-1}(\boldsymbol{S}^k)^T \boldsymbol{W}(\hat{\boldsymbol{\phi}} - \boldsymbol{\phi}(a^k)), \quad (29)$$

where the S is the sensitivity of the parameter a on the phase. It is expressed as

$$S = \frac{\partial\phi(a)}{\partial a}. \quad (30)$$

This quantity can be computed numerically using a finite difference scheme and by assuming a small variation of the diffusivity, i.e. 1%.
The algorithm can be initiated with a heat diffusivity of 1 mm^2/s as it is the order of magnitude for glass wafer.

6.2 Standard deviation

Once the diffusivity estimated, one can compute the associated standard deviation. From the standard deviation on the heat diffusivity is straightforward as

$$\sigma_a = \sigma_r \sqrt{[(\boldsymbol{S})^T \boldsymbol{W} \boldsymbol{S}]^{-1}} \tag{31}$$

with $\sigma_r = \sqrt{\mathcal{J}(a)/(N-1)}$ where N is the number of data points used to fit a. It is important to note that this standard deviation takes only into account the deviation between the measurement and the model, and the standard deviation on the measurements. However, several others bias in the measurement (position of the wafer, non linearity in the Peltier module during the heating...) can increase significantly this value.

7 Measurements

7.1 Experimental setting

Instructions to realise the thermal imaging in semi transparent media, and an estimate of the thermal diffusivity of a Borofloat sample are as follows:

1. Turn on all the instruments and set the chopper chopping frequency to $f_c \sim 10 - 12$ Hz. This value can be checked on the oscilloscope.

2. Set the waveform generator to trigger the camera. Two triggers need to be sent to the camera: one when the chopper is close, one when the chopper is open. The camera trigger needs therefore to be set at $2f_c \sim 20 - 24$ Hz.

3. Set the thermal modulation at 20 mHz with a voltage peak-peak value of 4 V. The electronic card powering the Peltier module converts this signal in current at the rate of 1 A/V. Use the second channel of the waveform generator to do so.

4. Once the periodic regime is established (after 10 min), record at least 10 thermal modulations to perform an accurate Fourier transform with at least a spectral resolution of 2 mHz.

7.2 Image processing

Once the set of a data is recorded, the data processing consists in two successive steps. First, the proper emission and transmitted signal needs to be separated. The images when the chopper is open and close are subtracted. A example of this signal are presented in Figure 8(a) and (b).

The variations of the transmitted signal over the recorded time is presented in Figure 8(c) for two pixels. Pixel 1, close to the edge where the wafer is heated, clearly shows a peak to peak modulation of 5×10^{-3}. Pixel 2, taken farther from the wafer edge, shows the same modulation but attenuated and shifted. This behaviour is expected. It is important to note here that a signal variation of only 1% is recorded at the maximum (pixel 1), corresponding to a variation of 80 DL over 8000 DL. This illustrates the weakness of the signal and justified the advanced metrology that needs to be used to be able to measure it properly.

The modulus of these signals, obtained by FFT, are presented in Figure 8(d). Two clear peaks at 20 mHz can be observed, validating the good result of the method. Such demodulation processing is extended to all the pixels of the images, and the fields at 20 mHz are extracted

for the parameter estimation.

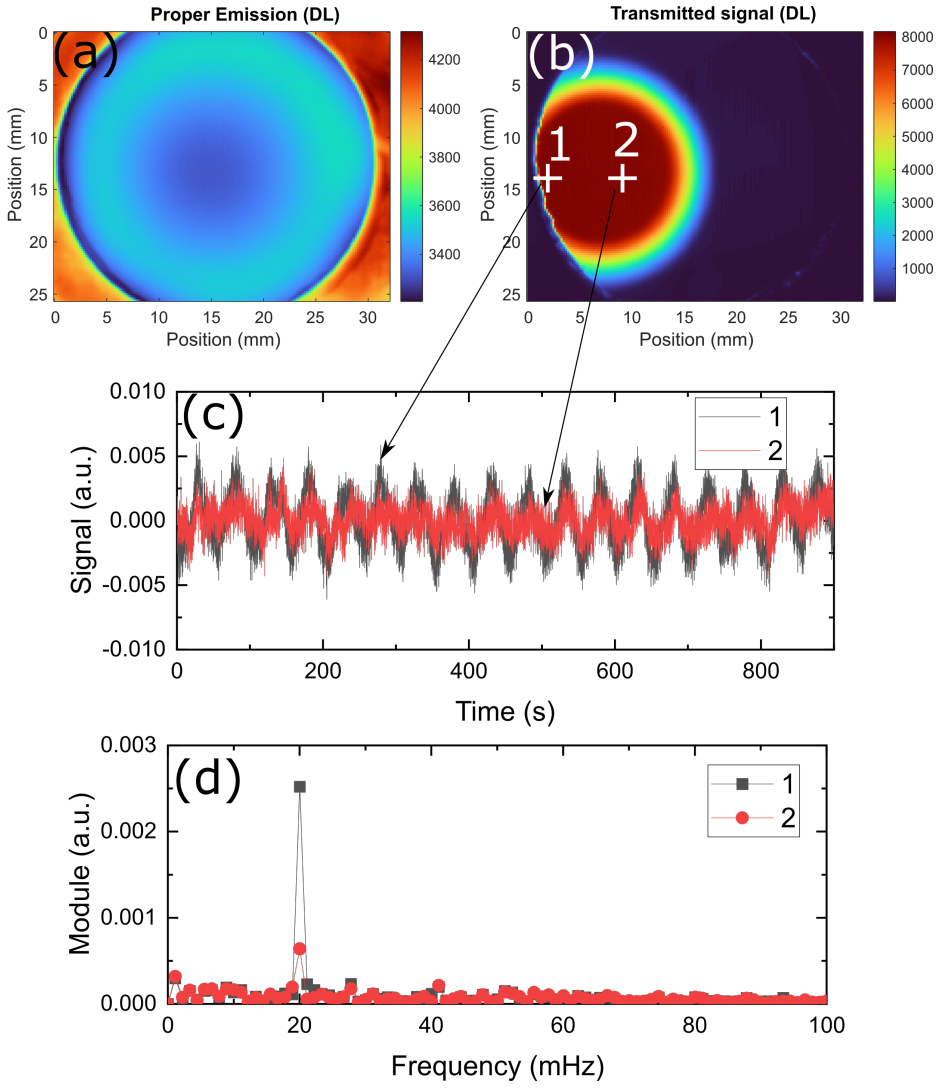

Figure 8: Image processing. (a) proper emission. (b) transmitted signal. (c) transmitted signal recorded during the experiment and divided by its mean. The location of the two pixels is indicated in (b). (d) associated fourier transform of the signal shown in (c).

7.3 Results

The modulus and phase fields obtained at 20 mHz are presented in Figure 9(a) and (b), respectively. Only the part of the image containing the IR beam (see Figure 8(b) for comparison) can be exploited. The rest of the image is only noise.

Both the modulus and the phase decrease from the edge of the wafer toward the center (between 2 and 15 mm in the image). Several artefacts are visible in the images. They are associated with the IR sensor itself, where small variations in the pixel reading by the camera electronics can be seen here. Usually, such artefacts are not visible when measurements with high SNR are performed.

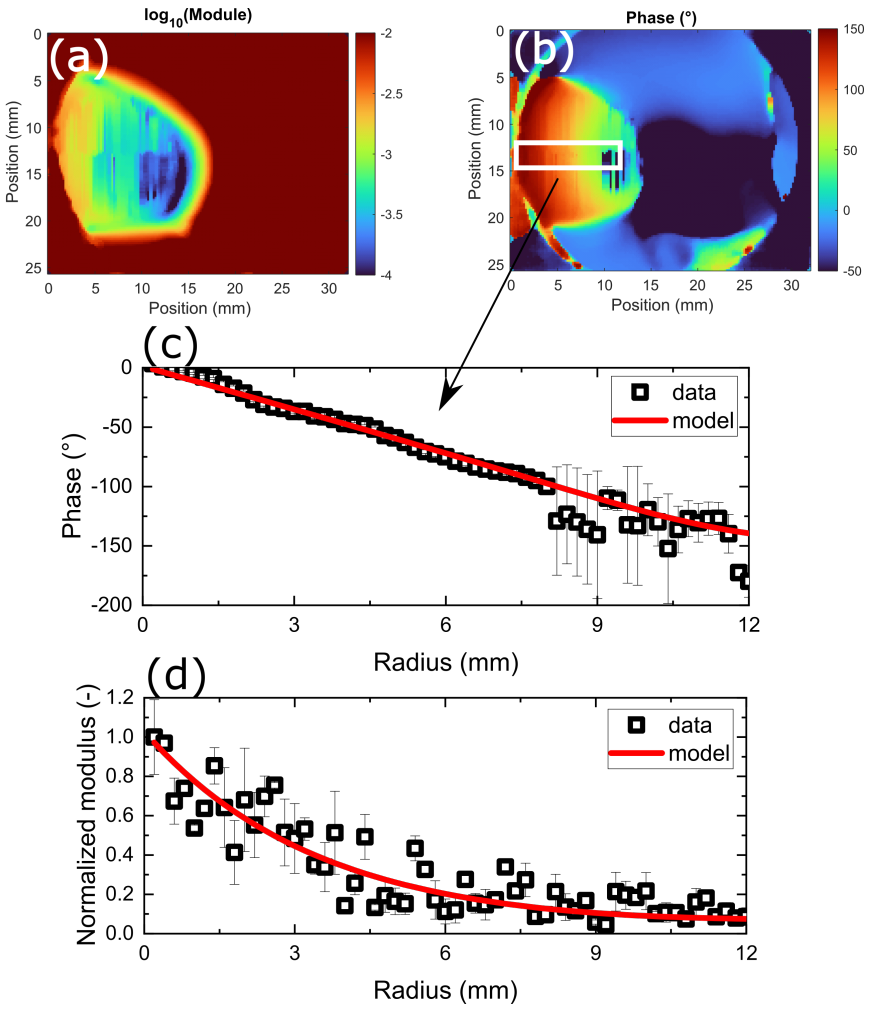

Figure 9: Image demodulation. (a) modulus of the thermotransmittance at 20 mHz. (b) the corresponding phase shift. (c) phase shift along a wafer radius average in the white rectangle in (b). (d) the corresponding modulus for the same location. A comparison with the model is done in (c) and (d).

In order to fit the thermal diffusivity, the data in the white rectangle are extracted and averaged along the vertical position (20 pixels) to obtain the phase versus the wafer radius. The error bar in the experimental data are related to the standard deviation over the average 20 pixels. Equation 29 is used to estimate the thermal diffusivity. The convection coefficient is taken to be 15 W/m^2/K, the wafer has a thickness of 500 µm, and the thermal conductivity of Borofloat is 1 W/m/K. The algorithm was able to converge in less than 10 iterations (see Figure 10). The tolerance limits was set to 10^{-6}.

The result of the fit can be seen in Figure 9(c). Overall a good agreement between the model and the data is observed, except when $r > 8$ mm where the IR sensor artefacts are visible. The estimated diffusivity is $a = (0.93 \pm 0.2)$ mm^2/s which is typically in the expected range for such glass wafer. A check on the modulus distribution is done through Figure 9, and here again, a excellent agreement between the model and data is obtained.

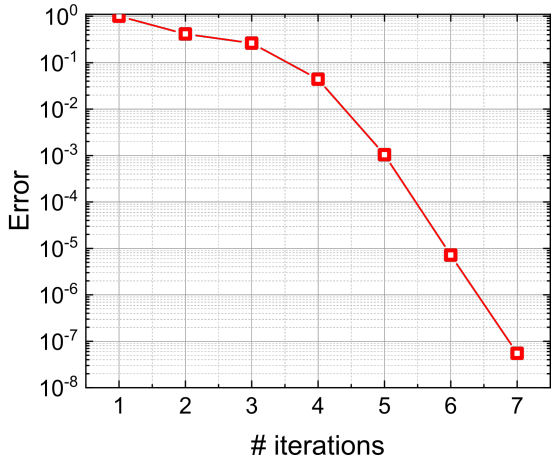

Figure 10: Convergence of the Gauss-Newton algorithm during the diffusivity estimation.

8 Conclusions

In this tutorial a new method to measure the temperature fields in semi-transparent media was introduced. Thermotransmittance enabled a contactless measurement of the mean temperature in semi-transparent media with the downside to be a very weak signal. Therefore, an advanced metrology was carried out, based on a double modulation of the signal recorded by the camera. Image processing in Matlab enabled to extract the thermotransmittance phase and modulus which were successfully used for parametric estimation. More detailed on the techniques can be found in the following publication [17].

Such technique can be extended to many other measurements ranging from optical properties characterisation, thermal microscopy, thermal characterization of heterogeneous materials, to 3D temperature fields measurements.

References

[1] J. Gieseler, A. Adibekyan, C. Monte, J. Hollandt, Apparent emissivity measurement of semi-transparent materials part 2: Theoretical concept, Journal of Quantitative Spectroscopy and Radiative Transfer 258 (2021) 107317. doi:10.1016/j.jqsrt.2020.107317. URL https://doi.org/10.1016/j.jqsrt.2020.107317

[2] S. Jeon, S.-N. Park, Y. S. Yoo, J. Hwang, C.-W. Park, G. W. Lee, Simultaneous measurement of emittance, transmittance, and reflectance of semitransparent materials at elevated temperature, Optics Letters 35 (23) (2010) 4015. doi:10.1364/ol.35.004015. URL https://doi.org/10.1364/ol.35.004015

[3] J. Gieseler, A. Adibekyan, C. Monte, J. Hollandt, Apparent emissivity measurement of semi-transparent materials part 1: Experimental realization, Journal of Quantitative Spectroscopy and Radiative Transfer 257 (2020) 107316. doi:10.1016/j.jqsrt.2020.107316. URL https://doi.org/10.1016/j.jqsrt.2020.107316

[4] O. Rozenbaum, D. D. S. Meneses, Y. Auger, S. Chermanne, P. Echegut, A spectroscopic method to measure the spectral emissivity of semi-transparent materials up to high temperature, Review of Scientific Instruments 70 (10) (1999) 4020–4025.

doi:10.1063/1.1150028.
URL https://doi.org/10.1063/1.1150028

[5] D. D. S. Meneses, P. Melin, L. del Campo, L. Cosson, P. Echegut, Apparatus for measuring the emittance of materials from far infrared to visible wavelengths in extreme conditions of temperature, Infrared Physics andTechnology 69 (2015) 96–101. doi:10.1016/j.infrared.2015.01.011.
URL https://doi.org/10.1016/j.infrared.2015.01.011

[6] A. Adibekyan, E. Kononogova, C. Monte, J. Hollandt, Review of PTB measurements on emissivity, reflectivity and transmissivity of semitransparent fiber-reinforced plastic composites, International Journal of Thermophysics 40 (4) (Mar. 2019). doi:10.1007/s10765-019-2498-0.
URL https://doi.org/10.1007/s10765-019-2498-0

[7] A. Philipp, N. W. Pech-May, B. A. F. Kopera, A. M. Lechner, S. Rosenfeldt, M. Retsch, Direct measurement of the in-plane thermal diffusivity of semitransparent thin films by lock-in thermography: An extension of the slopes method, Analytical Chemistry 91 (13) (2019) 8476–8483. doi:10.1021/acs.analchem.9b01583.
URL https://doi.org/10.1021/acs.analchem.9b01583

[8] E. A. A. Pogna, X. Jia, A. Principi, A. Block, L. Banszerus, J. Zhang, X. Liu, T. Sohier, S. Forti, K. Soundarapandian, B. Terrés, J. D. Mehew, C. Trovatello, C. Coletti, F. H. L. Koppens, M. Bonn, H. I. Wang, N. van Hulst, M. J. Verstraete, H. Peng, Z. Liu, C. Stampfer, G. Cerullo, K.-J. Tielrooij, Hot-carrier cooling in high-quality graphene is intrinsically limited by optical phonons, ACS Nano 15 (7) (2021) 11285–11295. doi:10.1021/acsnano.0c10864.
URL https://doi.org/10.1021/acsnano.0c10864

[9] M. Polyanskiy, Refractiveindex.info.
URL https://refractiveindex.info/

[10] C. Pradere, M. Ryu, A. Sommier, M. Romano, A. Kusiak, J. L. Battaglia, J. C. Batsale, J. Morikawa, Non-contact temperature field measurement of solids by infrared multispectral thermotransmittance, Journal of Applied Physics 121 (8) (2017) 085102. doi:10.1063/1.4976209.
URL https://doi.org/10.1063/1.4976209

[11] M. Bensalem, A. Sommier, J. C. Mindeguia, J. C. Batsale, L.-D. Patino-Lope, C. Pradere, Contactless transient THz temperature imaging by thermo-transmittance technique on semi-transparent materials, Journal of Infrared, Millimeter, and Terahertz Waves 39 (11) (2018) 1112–1126. doi:10.1007/s10762-018-0521-3.
URL https://doi.org/10.1007/s10762-018-0521-3

[12] N. Kakuta, Y. Fukuhara, K. Kondo, H. Arimoto, Y. Yamada, Temperature imaging of water in a microchannel using thermal sensitivity of near-infrared absorption, Lab on a Chip 11 (20) (2011) 3479. doi:10.1039/c1lc20261h.
URL https://doi.org/10.1039/c1lc20261h

[13] E. Hecht, Optics, 4th Edition, Addison Wesley, 2002.

[14] P. Linstrom, Nist chemistry webbook, nist standard reference database 69 (1997). doi:10.18434/T4D303.
URL http://webbook.nist.gov/chemistry/

[15] Y. Souhar, Caractérisation thermique de matériaux anisotropes à hautes températures, Theses, Institut National Polytechnique de Lorraine (May 2011).
URL https://hal.univ-lorraine.fr/tel-01749289

[16] M. Romano, M. Ryu, J. Morikawa, J. Batsale, C. Pradere, Simultaneous microscopic measurements of thermal and spectroscopic fields of a phase change material, Infrared Physics and Technology 76 (2016) 65–71. doi:10.1016/j.infrared.2016.01.010.
URL https://doi.org/10.1016/j.infrared.2016.01.010

[17] C. Bourges, S. Chevalier, J. Maire, A. Sommier, C. Pradere, S. Dilhaire, Infrared thermotransmittance-based temperature field measurements in semitransparent media, Review of Scientific Instruments 94 (3) (2023) 034905. doi:10.1063/5.0131422.
URL https://doi.org/10.1063/5.0131422